ACS NANO
Cite This: ACS Nano 2019, 13, 9198–9205
www.acsnano.org

ARTICLE

Single-Atom-Thick Active Layers Realized in Nanolaminated $Ti_3(Al_xCu_{1-x})C_2$ and Its Artificial Enzyme Behavior

Youbing Li,[†,‡] Mian Li,[†] Jun Lu,[§] Baokai Ma,[†,∥] Zhipan Wang,[∥] Ling-Zhi Cheong,[∥] Kan Luo,[†] Xianhu Zha,[†] Ke Chen,[†] Per O. Å. Persson,[§] Lars Hultman,[§] Per Eklund,[§] Cai Shen,[†] Qigang Wang,[⊥] Jianming Xue,[#] Shiyu Du,[†] Zhengren Huang,[†] Zhifang Chai,[†] and Qing Huang*[,†]

[†]Engineering Laboratory of Advanced Energy Materials, Ningbo Institute of Materials Technology and Engineering, Chinese Academy of Sciences, Ningbo, Zhejiang 315201, China
[‡]University of Chinese Academy of Sciences, 19 A Yuquan Road, Shijingshan District, Beijing 100049, China
[§]Department of Physics, Chemistry, and Biology (IFM), Linköping University, 58183 Linköping, Sweden
[∥]College of Food and Pharmaceutical Sciences, Ningbo University, Ningbo 315211, China
[⊥]Shool of Chemical Science and Engineering, Tongji University, Shanghai 200092, China
[#]State Key Laboratory of Nuclear Physics and Technology, School of Physics, Peking University, Beijing 100871, China

Supporting Information

ABSTRACT: **A $Ti_3(Al_xCu_{1-x})C_2$ phase with Cu atoms with a degree of ordering in the A plane is synthesized through the A site replacement reaction in $CuCl_2$ molten salt. The weakly bonded single-atom-thick Cu layers in a $Ti_3(Al_xCu_{1-x})C_2$ MAX phase provide actives sites for catalysis chemistry. As-synthesized $Ti_3(Al_xCu_{1-x})C_2$ presents unusual peroxidase-like catalytic activity similar to that of natural enzymes. A fabricated $Ti_3(Al_xCu_{1-x})C_2$/chitosan/glassy carbon electrode biosensor prototype also exhibits a low detection limit in the electrochemical sensing of H_2O_2. These results have broad implications for property tailoring in a nanolaminated MAX phase by replacing the A site with late transition elements.**

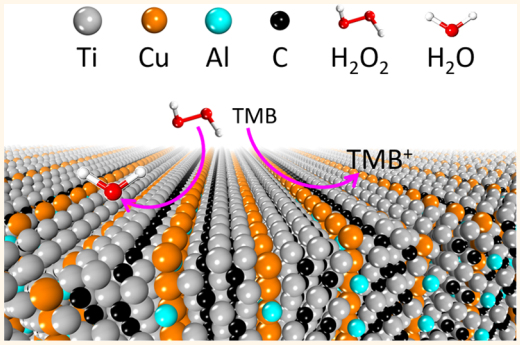

KEYWORDS: *nanolaminate, MAX phase, copper, catalysis, replacement reaction*

The $M_{n+1}AX_n$ phases are a family of nanolaminated compounds with hexagonal crystal structure.[1] The crystal structures of $M_{n+1}AX_n$ phases comprise MX slabs interleaved by single-atom-thick A layers (where M is an early transition metal, A is an element mostly from group 13 or 14, X is C and/or N, and n = 1−3). Generally, the mixed covalent and ionic M−X bond in MAX phases contributes to their high electrical/thermal conductivities and ceramic-like properties such as super-elastic stiffness. The comparatively weak M−A bond renders the MAX phases resistant to thermal shock and even irradiation damage.[2−6] Therefore, MAX phases have been investigated as promising structural materials in the environments of neutron radiation,[7] severe corrosion,[8] high temperature oxidation,[9,10] tribological properties,[11] and high-power electrical contacts.[12] However, until now the exploration of the functional application of MAX phases has been very limited.[13] Recently, noble-metal-containing MAX phases (Ti_3AuC_2 and Ti_3IrC_2) were synthesized by a substitution reaction through annealing.[14] These results indicate that highly stable Au and Ir atoms at the A site contribute to much improved electron transportation behavior of the MAX phases, resulting in excellent ohmic contact with the SiC substrate. In our recent study, a series of MAX phases with Zn at the A site were synthesized through an element replacement reaction approach from the traditional MAX phase in Lewis acidic molten salt (*i.e.*, $ZnCl_2$).[15] Because Ir, Au, and Zn belong to late transition metal elements (groups 9, 11, and 12, respectively), their outmost d-orbital electrons would expand the chemical space for tailoring the properties and functionality of MAX phases.

In the present communication, we have used a replacement reaction between Ti_3AlC_2 and $CuCl_2$ molten salt to synthesize a MAX phase where Cu atoms in the A layer show a degree of in-plane ordering. The alloying of Cu atoms in the Al sublayers

Received: May 7, 2019
Accepted: July 22, 2019
Published: July 22, 2019

Downloaded via UNIV OF ROCHESTER on March 3, 2020 at 17:13:08 (UTC).
See https://pubs.acs.org/sharingguidelines for options on how to legitimately share published articles.

© 2019 American Chemical Society

DOI: 10.1021/acsnano.9b03530
ACS Nano 2019, 13, 9198–9205

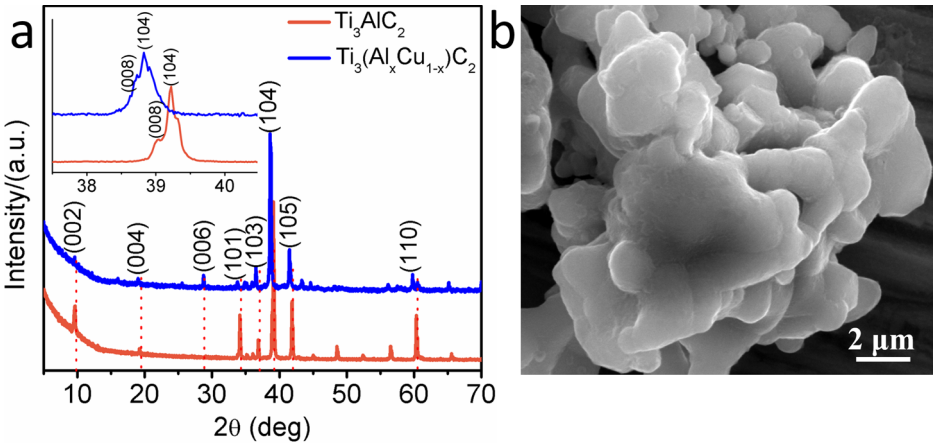

Figure 1. (a) XRD patterns of Ti_3AlC_2 and $Ti_3(Al_xCu_{1-x})C_2$. (b) SEM image of $Ti_3(Al_xCu_{1-x})C_2$.

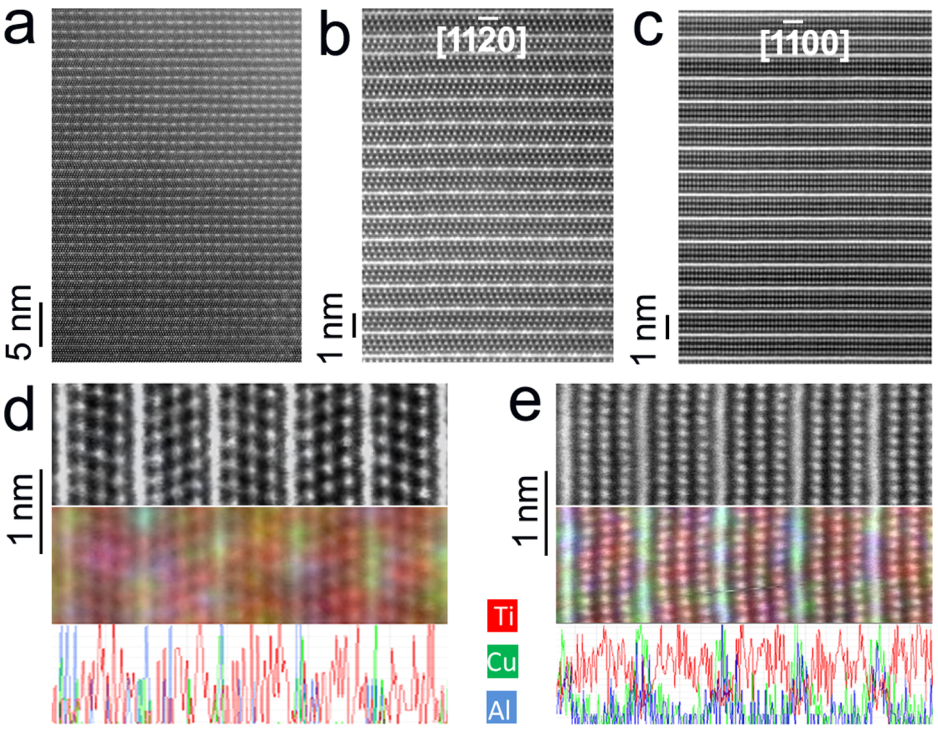

Figure 2. (a) High-resolution (HR)-STEM image of $Ti_3(Al_xCu_{1-x})C_2$. (b) Corresponding partial magnification from (a) showing atomic positions along the [11$\bar{2}$0] direction. (c) HR-STEM image of $Ti_3(Al_xCu_{1-x})C_2$ along the [1$\bar{1}$00] direction. The EDS mapping and line scan of Ti Kα (red), Cu Kα (green), and Al Kα (blue) signals of $Ti_3(Al_xCu_{1-x})C_2$ along [11$\bar{2}$0] (d) and [1$\bar{1}$00] (e).

in Ti_3AlC_2 follows a reaction that can be predicted thermodynamically from the Cu−Al phase diagram. The Cu atoms are theoretically predicted to weakly bond to the MX sublayers, thus weakly bonded single-atom-thick Cu layers in $Ti_3(Al_xCu_{1-x})C_2$ MAX phase provide reactive sites for potential catalysis chemistry. In fact, the as-synthesized $Ti_3(Al_xCu_{1-x})C_2$ phase exhibits unusual peroxidase-like catalytic activity, similar to that of natural enzymes. Moreover, a MAX/chitosan/glassy carbon electrodes (GCE) biosensor prototype also exhibited a very sensitive detection capability for H_2O_2.

RESULTS AND DISCUSSION

The $Ti_3(Al_xCu_{1-x})C_2$ phase was synthesized by a replacement reaction between Ti_3AlC_2 and $CuCl_2$ molten salt with a mole ratio of 1:1.5 at 700 °C. The X-ray diffraction peaks of the products are very close to that of Ti_3AlC_2, as shown in Figure 1a. Several specific peaks of the resulting phase, such as (103), (104), and (105), are shifted toward lower angles, indicating an expanded crystal lattice caused by the replacement of Al atoms with larger Cu atoms.[16] The (002) peak is almost vanished, and the (006) peak becomes strong, indicating a change in periodic symmetry along the *c* axis and the corresponding structure factor. Figure 1b shows a scanning electron microscopy (SEM) image of $Ti_3(Al_xCu_{1-x})C_2$. The morphology of product powders becomes less sharp at the edges when compared with the typical layered microstructure of the Ti_3AlC_2 materials (Figure S1a) and other MAX phases.[17] The atomic ratio of Ti/(Al+Cu)/C can be semiquantitatively estimated from energy-dispersive X-ray spectroscopy (EDS) results (Figure S1b) of powders and is close to 3:1:2, the stoichiometry of Ti_3AlC_2. Moreover, the

DOI: 10.1021/acsnano.9b03530
ACS Nano 2019, 13, 9198−9205

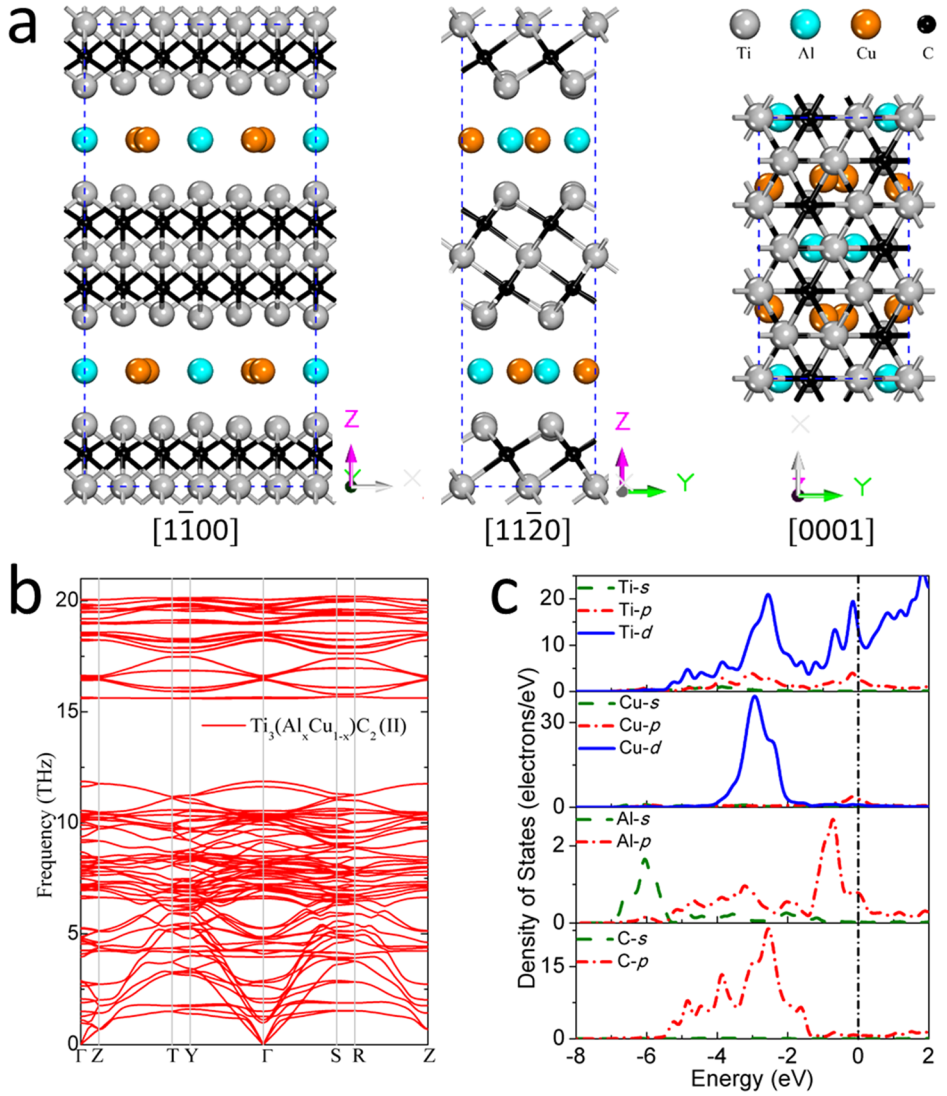

Figure 3. (a) Crystal model of $Ti_3(Al_{1/3}Cu_{2/3})C_2$ along and [1$\bar{1}$00], [11$\bar{2}$0], and [0001] directions. (b) Phonon dispersion of $Ti_3(Al_{1/3}Cu_{2/3})C_2$. (c) Projected density of states of $Ti_3(Al_{1/3}Cu_{2/3})C_2$.

relative atomic ratio of Al/Cu is about 1:2 (Table S1), which indicates that the as-synthesized MAX phase may have a chemical formula of $Ti_3(Al_{1/3}Cu_{2/3})C_2$.

The atomic structure and chemical analysis of $Ti_3(Al_{1/3}Cu_{2/3})C_2$ were further identified by high-resolution high-angle annular dark-field scanning transmission electron microscopy (HAADF-STEM) and a lattice-resolved energy-dispersive X-ray spectroscopy, as shown in Figure 2. A low-magnification STEM image of $Ti_3(Al_{1/3}Cu_{2/3})C_2$ clearly shows an in-plane ordering phenomenon, and some bright dots appear and have some periodic spacing between each other (Figure 2a). The exact atomic positions along the [11$\bar{2}$0] and [1$\bar{1}$00] orientations are shown in Figure 2b,c, respectively. The Ti_3C_2 sublayers in a newly fabricated MAX phase preserve the zigzag pattern with respect to each other and are separated by layers of the A element, which is brighter than the Ti element.[15] As the brightness of the atom is dependent on its mass (intensity ~ Z^2), it can be confirmed that the Cu atoms have replaced Al atoms in the A layers (Figure 2a,b). The Cu atoms appear to exhibit a degree of ordering, in contrast to the Au and Zn cases where the A element is completely replaced.[15,18,19] A lattice-resolved EDS map and a line scan that reveal the elemental distribution of $Ti_3(Al_{1/3}Cu_{2/3})C_2$ are shown in Figure 2d,e, respectively. The relative atomic ratio of Al to Cu is about 1:2 as identified by STEM-EDS (Table S2). The continuous bright line shown in the STEM image along [1$\bar{1}$00] further indicates that the Cu atoms occupy the A atomic layer, but it is difficult to resolve atomically, similar to Zn-containing MAX phases.[15]

The formation of a Cu−Al layer with short-distance ordering in the MAX phase is intriguing when compared with the complete replacement of MAX phases by Zn and Au atoms.[15,18] It should follow a similar chemical reaction, in which molten $CuCl_2$ thermodynamically reacts with Al atoms in Ti_3AlC_2 and generates both Cu and $AlCl_3$ in the initial stage. $AlCl_3$ quickly evaporates due to its low boiling point (~180 °C), which will allow Cu atoms to occupy the lattice vacancies left by Al. This will initially occur on the Ti_3AlC_2 surface to maintain the structural integrity and to form the substitutional defect of Cu_{Al}. The continuous Cu substitution at the basal plane is attributed to two reasons. First, at a synthesis temperature of 700 °C, the trigonal prism space between two neighboring MX sublayers expands enough for movement of thermally activated Al and Cu atoms. Second, in the binary

DOI: 10.1021/acsnano.9b03530
ACS Nano 2019, 13, 9198−9205

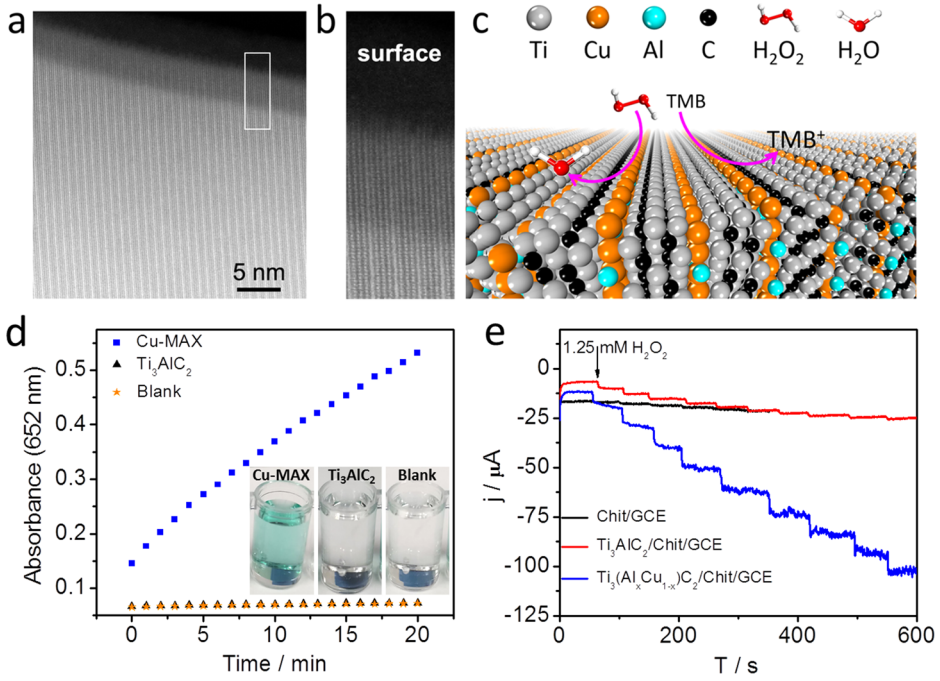

Figure 4. (a) STEM image of $Ti_3(Al_xCu_{1-x})C_2$ along the $[1\bar{1}00]$ orientation showing the exposed Cu atoms (bright lines) and (b) enlarged STEM image near the surface of particle. (c) Simulated surface atomic configuration for peroxidase-like catalysis. (d) Time-dependent absorbance evolution at 652 nm of blank solution, Ti_3AlC_2, and Cu-MAX-catalyzed TMB oxidation. The inset shows the optical photographs of TMB solution following oxidation by Ti_3AlC_2, Cu-MAX, and HRP; the reaction temperature is 37 °C. (e) Amperometric responses of chitosan/GCE, Cu-MAX/chitosan/GCE and Ti_3AlC_2/chitosan/GCE at −0.9 V upon successive additions of 1.25 mM H_2O_2 in stirred 0.1 M PBS (pH 7.0).

phase diagram, Al and Cu (lower than 40 atom % of Cu) can form a liquid solution as their lowest eutectic point is 548 °C (Figure S2), meaning the mutual diffusion of Al and Cu atoms is favorable. Thus, both kinetic and thermodynamic factors are satisfied for the in-diffusion of Cu atoms and the out-diffusion of Al atoms in the MAX phase. When inner Al atoms diffuse to the surface, they will soon be oxidized by Lewis acid Cu^{2+} and form gaseous $AlCl_3$ until the composition of Al−Cu in the A layer reaches the solid phase zone. According to the Al−Cu phase diagram, when the concentration of Cu in the Al layer reaches 40 atom %, solid intermetallic phases are formed. In the Zn−Al and Au−Si binary phase diagram, there are two metal end-members that have limited dissolution with each other below a low solidus line, which explains why nearly pure MAX (A = Zn and Au) phases[14,15,20] are achieved if Al atoms can be fully driven out. In the case of the Cu−Al binary system, there are intermediate alloy phases between these two metal end-members. The nucleation of intermediate Cu−Al alloy phases at a high concentration of Cu in Al would solidify the liquid alloy. It can also be determined from the Cu−Al phase diagram that the Cu atomic percentage of ε phase at 700 °C is about 56.7 atom %, close to the experimental result of 66 atom % of Cu in the A site of $Ti_3(Al_{1/3}Cu_{2/3})C_2$. The above explanation is reasonable when Cu and Al atoms stay in a weakly bonding space that resembles the three-dimensional alloying condition. However, the bonding strength between the M and A elements will also influence the alloying behavior of atoms in the A layer.

First-principles density functional calculations were performed in order to investigate the structure of $Ti_3(Al_{1/3}Cu_{2/3})C_2$ and its stability. A lattice-symmetry-preserved structure model formed by simply replacing two-thirds of Al in Ti_3AlC_2 with Cu was found to be unstable, as evident imaginary frequencies appear (Figure S3). Instead, Figure 3a shows a stable configuration was achieved by allowing the symmetry to be broken. It should be stressed that this proposed lattice structure is an approximation of the observed ordering of the Cu and Al in the A layer. Interestingly, in such a stable $Ti_3(Al_{1/3}Cu_{2/3})C_2$ configuration, the Cu(Al) site deviates from the original A site (0, 0, 1/4) and toward to the rectangle center of the neighboring four Ti atoms. The corresponding total energy of this configuration shows an energy 0.39 eV lower than that in the hypothetical structure where Cu precisely stays at the original Al sites. The front, side, and top views of this configuration are presented in Figure 3a. The deviation of the A site element is consistent with symmetry reduction in the $Ti_3(Al_{1-\delta}Cu_\delta)C_2$ MAX phase reported previously,[21] and it also explains the blurred Cu atom distribution as shown in the STEM image (Figure 2c). Figure 3b,c shows the corresponding phonon dispersion and projected density of states (PDOS) of this configuration. The structure is dynamically stable, as no imaginary frequencies are observed in the phonon dispersion. From the partial DOS, the conductive behavior of $Ti_3(Al_{1/3}Cu_{2/3})C_2$ is metallic, and the DOS in the vicinity of the Fermi level is mainly contributed by the Ti d-, Cu p-, and Al p-orbitals (Figure S4). The calculated structure parameters are also presented in Table S3. The elastic parameters in $Ti_3(Al_{1/3}Cu_{2/3})C_2$ are much lower than those in Ti_3AlC_2, and the cleavage energy of 1.528 J/m^2 between the Ti−Cu(Al) interface is much lower than that of the Ti−Al surface in Ti_3AlC_2 (1.934 J/m^2). The decreased elastic constants and cleavage energy of the Cu-substituted configuration also explain the symmetry reduction along the *c* axis (Figure 1a). In Ti_3AlC_2, the Al atom is six-coordinated, and the bond length of Ti−Al is calculated to be 2.890 Å. However, due to the four

DOI: 10.1021/acsnano.9b03530
ACS Nano 2019, 13, 9198−9205

coordination in $Ti_3(Al_{1/3}Cu_{2/3})C_2$, the nearest bond length of Ti−Cu is calculated as 2.753 Å, and the next-nearest Ti−Cu(Al) bond length is larger than 3.279 Å, which makes Cu atoms more free than in the six-coordinated site. Because Cu has more outermost d-orbital valence electrons than Al, the $Ti_3(Al_{1/3}Cu_{2/3})C_2$ could provide many active atoms for further chemical reaction, such as catalysis.

It is expected that the exposed Cu atoms on the surface of the as-synthesized $Ti_3(Al_{1/3}Cu_{2/3})C_2$ MAX phase (Figure 4a,b) could provide active sites of single-atom-thick Cu layers for catalysis. The STEM image indicates the particles have a clean surface without an amorphous phase (Figure 4a,b). Thus, the single-atom Cu should be exposed to environment, as illustrated in a simulated surface atomic configuration (Figure 4c). Actually, the as-synthesized $Ti_3(Al_{1/3}Cu_{2/3})C_2$ MAX phase can strongly accelerate H_2O_2 solution and release O_2, whereas the control Ti_3AlC_2 MAX phase shows no such phenomenon (Videos S1 and S2 in the Supporting Information). The peroxidase-like activity of $Ti_3(Al_{1/3}Cu_{2/3})C_2$ was further tested in terms of oxidations of chromogenic 3,3′,5,5′-tetramethylbenzidine (TMB). It was revealed that $Ti_3(Al_{1/3}Cu_{2/3})C_2$ is able to oxidize TMB in the presence of H_2O_2 in a manner similar to the peroxidative ability of horseradish peroxidase (HRP),[22] resulting in a blue-colored solution with a maximum absorbance at 652 nm, like other enzyme catalytic materials.[23,24] Figure 4d shows the time-dependent absorbance evolution at 652 nm of blank solution, Ti_3AlC_2, and $Ti_3(Al_{1/3}Cu_{2/3})C_2$ for TMB oxidation. $Ti_3(Al_{1/3}Cu_{2/3})C_2$ demonstrated a tremendous increasing absorbance value with reaction time, which is similar to that of HRP (Figure S5), whereas Ti_3AlC_2 and the blank sample show no obvious peroxidase-like catalytic activity even after 20 min. Cu-MAX also demonstrated higher temperature stability in comparison to that of HRP. Following 20 min of reaction at 80 °C, Cu-MAX showed significant lesser decrease in absorbance value as compared to that with HRP (Figure S6). In addition, Cu-MAX also demonstrated good catalytic stability and ability to maintain 98.03 ± 0.26% of its initial catalytic activity after five consecutive reactions (Figure S7). The steady-state kinetic parameters for both HRP and $Ti_3(Al_{1/3}Cu_{2/3})C_2$ were examined, and Lineweaver−Burk plots showed good linear relationship with parallel lines (Figure S8), indicating characteristics of a ping-pong mechanism similar to that of the natural HRP enzyme[25] or Fe_3O_4 artificial enzyme.[26] A comparison of the HRP and $Ti_3(Al_{1/3}Cu_{2/3})C_2$ kinetic parameters obtained from the Michaelis−Menten and Lineweaver−Burk plots is shown in Table S4. K_m values are an indication of enzyme affinity toward substrates. A small K_m value indicates high affinity between the enzyme and the substrates and *vice versa*. The observed K_m (0.512 mM) value of $Ti_3(Al_{1/3}Cu_{2/3})C_2$ with H_2O_2 substrate is found to be smaller than that of the HRP enzyme (1.611 mM), suggesting that the Cu-MAX phase possesses higher affinity of the catalyst for H_2O_2.[27] It is possible that $Ti_3(Al_{1/3}Cu_{2/3})C_2$ possesses more active sites on the surface, whereas HRP has only one active site per molecule. Regarding the catalase behavior observed in $Ti_3(Al_{1/3}Cu_{2/3})C_2$, H_2O_2 must adsorb on the surface of $Ti_3(Al_{1/3}Cu_{2/3})C_2$ particles, and the O−O bond of H_2O_2 can be broken up into double hydroxyl radical (•OH) radical by exposed surface of Cu atom layers in the MAX phase. Electron spin resonance (ESR) results suggest that the decomposition of H_2O_2 with concomitant formation of •OH in the presence of $Ti_3(Al_{1/3}Cu_{2/3})C_2$ (Figure S9),[28] and the phase composition of $Ti_3(Al_{1/3}Cu_{2/3})C_2$ is unchanged after reaction with H_2O_2 (Figure S10). In addition, X-ray photoelectron spectra (XPS) results imply the presence of an unfilled Cu $3d^9$ shell and thus confirms the existence of Cu^{2+} on the sample surface (Figure S11).[29,30] Thus, we supposed that the catalytic ability of $Ti_3(Al_{1/3}Cu_{2/3})C_2$ might be attributed to oxidation of surface-exposed Cu atoms by H_2O_2. These •OH are generated in the reaction between H_2O_2 and surface oxidation Cu atom layers in $Ti_3(Al_{1/3}Cu_{2/3})C_2$, and released •OH oxidized TMB to form blue-colored TMB^+, like Cu nanoclusters.[29] It is well-known that copper is soluble in concentrated nitric acid; compared to an artificial nanozyme of Cu nanoclusters,[31] bulk $Ti_3(Al_{1/3}Cu_{2/3})C_2$ MAX phase with particle size of several micrometers (about 2 μm) is employed (Figure S12 and Table S5), which shows structure stability in an acid corrosive environment (*e.g.*, concentrated nitric acid (Figure 1a), concentrated hydrochloric acid (Figure S13), *etc.*).

The peroxidase-like catalytic activity of $Ti_3(Al_{1/3}Cu_{2/3})C_2$ may find application in the detection of H_2O_2 in food, biology, medicine, and the environment fields. Figure 4e shows the amperometric responses of $Ti_3(Al_{1/3}Cu_{2/3})C_2$/chitosan/GCE and Ti_3AlC_2/chitosan/GCE following successive additions of H_2O_2 to phosphate buffer. Unlike chitosan/GCE and Ti_3AlC_2/chitosan/GCE, $Ti_3(Al_{1/3}Cu_{2/3})C_2$/chitosan/GCE yielded an obvious step-like response of current following successive additions of H_2O_2 to phosphate buffer, showing linear regression behavior in the concentration range from 0.06 to 11.25 μM (Figure S14). A low limit of detection (LOD) of 0.06 μM was achieved, which is much lower than that of CuO,[30] Cu NCs,[31] Au NPs,[32] Pt,[33] Ag NPs,[34] and Pd[35] (Table S6). Moreover, the catalytic activity of nanoparticles gradually deteriorates due to Ostwald ripening. However, in the $Ti_3(Al_{1/3}Cu_{2/3})C_2$ MAX phase, active Cu atoms isolated by MX sublayers should avoid such poisoning grain growth, which also explains that the micrometer-sized particles of the MAX phase still preserve the catalytic activity.

CONCLUSIONS

In summary, a $Ti_3(Al_{1/3}Cu_{2/3})C_2$ MAX phase, where Cu atoms partially occupy the A layer with a degree of ordering, was synthesized through a replacement approach. Due to the outermost d-orbital electrons of Cu, the bulk $Ti_3(Al_{1/3}Cu_{2/3})C_2$ phase provides a large amount of catalytically active sites in single-atom layers, resulting in unusual peroxidase-like catalytic activity similar to natural enzymes. An electrochemical biosensor with wide linear range and low limit of detection was fabricated in a MAX/chitosan/GCE prototype electrode. The active sites of Cu atoms and conductive MX sublayers account for the high detection capability. It is thus expected that other transition element atoms (such as Pt, Ag, Au, *etc.*) can similarly occupy A layer sites and form other types of active single-atom-thick layers in MAX phases and enable tailoring of chemical properties and functionality.

METHODS

Preparation of the Cu-MAX Phase. The Ti_3AlC_2 powders were synthesized by a molten salt method, as in our previous work.[15] The Ti_3AlC_2 powders were mixed with $CuCl_2$ in stoichiometric molar ratios of 2:3. Then, the mixed powders were put into an aluminum oxide boat and heated to 700 °C during 2 h with a heating rate of 10 °C/min under an argon atmosphere. After the end of the reaction, the surplus Cu was removed by immersing it in nitric acid for about 15

DOI: 10.1021/acsnano.9b03530
ACS Nano 2019, 13, 9198−9205

min. Finally, the product was filtered, washed, and dried at 40 °C in vacuum.

Peroxidase-like Catalytic Activity of Cu-MAX. Peroxidase-like activity of Cu-MAX was evaluated in terms of its ability to oxidize typical HRP substrate 3,3′,5,5′-tetramethylbenzidine in the presence of H_2O_2. The reaction was carried out at 37 and 80 °C by using 4 μg/mL of HRP or Cu-MAX in 10.0 mL reaction substrates containing 496.5 μM TMB and 0.38 M H_2O_2. The blue color that developed as the reaction proceeded was monitored in time scan mode at 652 nm using an Infinite 200 PRO multimode plate reader (Tecan, Switzerland). Control experiments were conducted in the absence of HRP or Cu-MAX. The steady-state kinetics were conducted using standard reaction conditions as described above by varying concentrations of TMB at a fixed concentration of H_2O_2 or *vice versa*. Kinetics parameters were determined by fitting reaction data to the Michaelis–Menten (eq 1) and Lineweaver–Burk (eq 2) equations.

$$\frac{1}{V} = \frac{K_m}{V_{max}} \times \frac{1}{[S]} + \frac{1}{V_{max}} \quad (1)$$

$$V = V_{max} \times \frac{[S]}{[S] + K_m} \quad (2)$$

where V is the reaction velocity, V_{max} is the maximal reaction velocity, $[S]$ is the substrate concentration (H_2O_2 or TMB), and K_m is the Michaelis–Menten constant.

Fabrication of the Cu-MAX/Chitosan/GCE and Ti_3AlC_2/Chitosan/GCE Electrochemical Sensor. Glassy carbon electrodes (3 mm) were polished using alumina oxide powder (1.0, 0.3, 0.05 μm), cleaned by ethanol and water, and dried under a gentle N_2 stream. Three hundred microliters of Cu-MAX or Ti_3AlC_2 aqueous solution (30 mg/mL) was mixed with 100 μL of chitosan solution (6 mg/mL) for 5 min. Five microliters of the $Ti_3(Al_{1/3}Cu_{2/3})C_2$/chitosan or Ti_3AlC_2/chitosan mixture solution was drop-cast onto the GCE surface.

Electrochemical Sensing of H_2O_2 by Cu-MAX/Chitosan/GCE and Ti_3AlC_2/Chitosan/GCE. Electrochemical sensing of H_2O_2 by Cu-MAX/chitosan/GCE and Ti_3AlC_2/chitosan/GCE was carried out using a CHI760E electrochemical workstation (Chenhua, Shanghai) with GCE (Cu-MAX/chitosan/GCE or Ti_3AlC_2/chitosan/GCE) as the working electrode, platinum wire as the counter electrode, and saturated calomel electrode as the reference electrode. Amperometric current–time curves for H_2O_2 were carried out to construct a calibration curve of current response at different H_2O_2 concentrations. Measurements were performed in 10 mL of stirred 0.1 M PBS (pH 7.0) with successive addition of H_2O_2 at room temperature under an applied peak potential value of −0.9 V.

The LOD was determined according to the following equation:

$$LOD = 3SD/K$$

where SD refers to the standard deviation of the control measurement and K refers to the slope of the calibration curve.

Density Functional Theory Calculations. All of the structural, electronic, and mechanical properties of the MAX phases investigated in our work were calculated in the plane-wave CASTEP[36,37] software. The ultrasoft pseudopotential with a plane-wave cutoff energy of 500 eV was adopted. The generalized gradient approximation of the Perdew–Berke–Ernzerhof scheme was employed for the exchange-correlation functional.[38−41] All of the structures were relaxed until the total energy change was smaller than 5×10^{-6} eV/atom, and the force on each atom was below 0.001 eV/Å. A k-point mesh of 13 × 13 × 2 was utilized for the unit cell of MAX phase, and an approximately equivalent k-point density was adopted for the Cu-substituted $Ti_3(Cu_{2/3}Al_{1/3})C_2$ state. Both relaxations that keep structure symmetry and those without symmetry were considered. To test the structural dynamical stability, phonon dispersions were calculated based on the finite displacement approach.[42,43] Elastic constants were calculated based on the stress–strain relationship, and then the shear (G) and Young's modulus (E) were obtained from the Voigt–Reuss–Hill approximation. In order to investigate the adhesive strengths between the M–A sublayers of MAX phases before and after Cu substitution, the cleavage energies were calculated. The definition of cleavage energy is $E = (E_{broken} - E_{bulk})/S$,[44] where E_{bulk} is the total energy of bulk MAX phase after optimization and E_{broken} denotes the corresponding total energy of a configuration with a vacuum separation of 10 Å between the M and A atomic layers in the previous bulk MAX; S is the surface area of the cleavage surface.

Characterization. The phase composition of the samples was analyzed by X-ray diffraction (D8 Advance, Bruker AXS, Germany) with Cu Kα radiation. The microstructure and chemical composition were observed by scanning electron microscopy (QUANTA 250 FEG, FEI, USA) coupled with an energy-dispersive spectrometer. The chemical state of the materials before and after exfoliation was analyzed by X-ray photoelectron spectroscopy (AXISUltra DLD, Kratos, Japan). The ESR measurements were carried out using a Bruker EMX ESR (A300-10/12, Sigma, Germany) spectrometer operating at 9.853 GHz (microwave power = 19.27 mW, modulation frequency = 100 kHz, modulation amplitude = 1.00 G, receiver gain = 1.00×10^3) with DMPO as the capturer in dark conditions (room temperature). The particle size of $Ti_3(Al_{1/3}Cu_{2/3})C_2$ was determined by a particle size analyzer (Microtrac, S3500-special, USA). Structural and chemical analyses were carried out by high-resolution STEM high-angle annular dark-field imaging and STEM-affiliated energy-dispersive X-ray spectroscopy within Linköping's double-C_s-corrected FEI Titan3 60-300 microscope operated at 300 kV, and STEM-EDS was recorded with the embedded high sensitivity super-X EDS detector.

ASSOCIATED CONTENT

Supporting Information

The Supporting Information is available free of charge on the ACS Publications website at DOI: 10.1021/acsnano.9b03530.

SEM image of Ti_3AlC_2, EDS analysis results of $Ti_3(Al_{1/3}Cu_{2/3})C_2$, average chemical composition, Cu–Al binary phase diagram, phonon dispersion, and crystal model of $Ti_3(Al_{1/3}Cu_{2/3})C_2$ (I), PDOS analysis of $Ti_3(Al_{1/3}Cu_{2/3})C_2$ (II), absorbance evolution of HRP, steady-state kinetic assays of HRP and $Ti_3(Al_{1/3}Cu_{2/3})C_2$, absorbance evolution of HRP $Ti_3(Al_{1/3}Cu_{2/3})C_2$ at 80 °C, electron spin resonance spectra, relative catalytic activity of the Cu-MAX phase, XRD patterns of $Ti_3(Al_{1/3}Cu_{2/3})C_2$ before and after the reaction with H_2O_2, X-ray photoelectron spectra of $Ti_3(Al_{1/3}Cu_{2/3})C_2$, particle size distribution of the $Ti_3(Al_{1/3}Cu_{2/3})C_2$, XRD patterns of $Ti_3(Al_{1/3}Cu_{2/3})C_2$ before and after the reaction with concentrated hydrochloric acid, calibration curve of amperometric responses, and other materials' detection limit for H_2O_2 (PDF)

Video S1: Reaction between MAX phase and H_2O_2 solution (MP4)

Video S2: Reaction between nanosized metal particles and H_2O_2 solution (MP4)

AUTHOR INFORMATION

Corresponding Author

*E-mail: huangqing@nimte.ac.cn.

ORCID

Mian Li: 0000-0002-3139-7456

Kan Luo: 0000-0002-8639-6135

Per O. Å. Persson: 0000-0001-9140-6724

Per Eklund: 0000-0003-1785-0864

Cai Shen: 0000-0001-5825-4028

Qigang Wang: 0000-0002-4026-3337

Shiyu Du: 0000-0001-6707-3915

DOI: 10.1021/acsnano.9b03530
ACS Nano 2019, 13, 9198−9205

Qing Huang: 0000-0001-7083-9416

Author Contributions

Q.H. conceived and initiated the work. Y.L. synthesized the materials. J.L. performed and analyzed the STEM results. P.O.Å.P., L.H., and P.E. contributed to the discussion of STEM results. B.M., Z.W., Q.W., and L.-Z.C. performed the peroxidase-like catalytic activity and electrochemical sensing of H_2O_2 measurement. K.L., X.Z., and S.D. performed the theoretical calculation. M.L., K.C., C.S., J.X., Z.H., and Z.C. contributed to the scientific discussion.

Notes

The authors declare no competing financial interest.

ACKNOWLEDGMENTS

This study was supported financially by the National Natural Science Foundation of China (Grant Nos. 21671195 and 91426304). The Knut and Alice Wallenberg Foundation is acknowledged for support of the electron microscopy laboratory in Linköping (Grant KAW 2015.0043), a Scholar Grant (L.H.), and a Fellowship grant (P.E.). P.O.Å.P. and J.L. acknowledge the Swedish Foundation for Strategic Research (EM16-0004) and the Research Infrastructure Fellow RIF 14-0074. We also acknowledge the Swedish Government Strategic Research Area in Materials Science on Functional Materials at Linköping University (Faculty Grant SFO-Mat-LiU No. 2009 00971).

REFERENCES

(1) Barsoum, M. W. The $M_{N+1}AX_N$ phases: A New Class of Solids: Thermodynamically Stable Nanolaminates. *Prog. Solid State Chem.* **2000**, *28*, 201−281.

(2) Eklund, P.; Beckers, M.; Jansson, U.; Högberg, H.; Hultman, L. The $M_{n+1}AX_n$ Phases: Materials Science and Thin-Film Processing. *Thin Solid Films* **2010**, *518*, 1851−1878.

(3) Sun, Z. M. Progress in Research and Development on MAX Phases: A Family of Layered Ternary Compounds. *Int. Mater. Rev.* **2011**, *56*, 143−166.

(4) Barsoum, M. W.; Radovic, M. Elastic and Mechanical Properties of the MAX Phases. *Annu. Rev. Mater. Res.* **2011**, *41*, 195−227.

(5) Zhang, H. B.; Zhou, Y. C.; Bao, Y. W.; Li, M. S. Abnormal Thermal Shock Behavior of Ti_3SiC_2 and Ti_3AlC_2. *J. Mater. Res.* **2006**, *21*, 2401−2407.

(6) Whittle, K. R.; Blackford, M. G.; Aughterson, R. D.; Moricca, S.; Lumpkin, G. R.; Riley, D. P.; Zaluzec, N. J. Radiation Tolerance of $M_{n+1}AX_n$ Phases, Ti_3AlC_2 and Ti_3SiC_2. *Acta Mater.* **2010**, *58*, 4362−4368.

(7) Tallman, D. J.; Hoffman, E. N.; Caspi, E. a. N.; Garcia-Diaz, B. L.; Kohse, G.; Sindelar, R. L.; Barsoum, M. W. Effect of Neutron Irradiation on Select MAX Phases. *Acta Mater.* **2015**, *85*, 132−143.

(8) Ward, J.; Bowden, D.; Prestat, E.; Holdsworth, S.; Stewart, D.; Barsoum, M. W.; Preuss, M.; Frankel, P. Corrosion Performance of Ti_3SiC_2, Ti_3AlC_2, Ti_2AlC and Cr_2AlC MAX Phases in Simulated Primary Water Conditions. *Corros. Sci.* **2018**, *139*, 444−453.

(9) Lin, Z. J.; Li, M. S.; Wang, J. Y.; Zhou, Y. C. High-Temperature Oxidation and Hot Corrosion of Cr_2AlC. *Acta Mater.* **2007**, *55*, 6182−6191.

(10) Wang, B.; Zhou, A.; Hu, Q.; Wang, L. Synthesis and Oxidation Resistance of V_2AlC Powders by Molten Salt Method. *Int. J. Appl. Ceram. Technol.* **2017**, *14*, 873−879.

(11) Zhu, Y.; Zhou, A.; Ji, Y.; Jia, J.; Wang, L.; Wu, B.; Zan, Q. Tribological Properties of Ti_3SiC_2 Coupled with Different Counterfaces. *Ceram. Int.* **2015**, *41*, 6950−6955.

(12) Fashandi, H.; Andersson, M.; Eriksson, J.; Lu, J.; Smedfors, K.; Zetterling, C. M.; Lloyd Spetz, A.; Eklund, P. Single-Step Synthesis Process of Ti_3SiC_2 Ohmic Contacts on 4H-SiC by Sputter-Deposition of Ti. *Scr. Mater.* **2015**, *99*, 53−56.

(13) Ng, W. H. K.; Gnanakumar, E. S.; Batyrev, E.; Sharma, S. K.; Pujari, P. K.; Greer, H. F.; Zhou, W.; Sakidja, R.; Rothenberg, G.; Barsoum, M. W.; Shiju, N. R. The Ti_3AlC_2 MAX Phase as an Efficient Catalyst for Oxidative Dehydrogenation of n-Butane. *Angew. Chem., Int. Ed.* **2018**, *57*, 1485−1490.

(14) Fashandi, H.; Dahlqvist, M.; Lu, J.; Palisaitis, J.; Simak, S. I.; Abrikosov, I. A.; Rosen, J.; Hultman, L.; Andersson, M.; Lloyd Spetz, A.; Eklund, P. Synthesis of Ti_3AuC_2, $Ti_3Au_2C_2$ and Ti_3IrC_2 by Noble Metal Substitution Reaction in Ti_3SiC_2 for High-Temperature-Stable Ohmic Contacts to SiC. *Nat. Mater.* **2017**, *16*, 814−818.

(15) Li, M.; Lu, J.; Luo, K.; Li, Y.; Chang, K.; Chen, K.; Zhou, J.; Rosen, J.; Hultman, L.; Eklund, P.; Persson, P. O. Å.; Du, S. Y.; Chai, Z. F.; Huang, Z. R.; Huang, Q. Element Replacement Approach by Reaction with Lewis Acidic Molten Salts to Synthesize Nanolaminated MAX Phases and MXenes. *J. Am. Chem. Soc.* **2019**, *141*, 4730−4737.

(16) Nechiche, M.; Gauthier-Brunet, V.; Mauchamp, V.; Joulain, A.; Cabioc'h, T.; Milhet, X.; Chartier, P.; Dubois, S. Synthesis and Characterization of a New $(Ti_{1-\varepsilon},Cu_\varepsilon)_3(Al,Cu)C_2$ MAX Phase Solid Solution. *J. Eur. Ceram. Soc.* **2017**, *37*, 459−466.

(17) He, H.; Jin, S.; Fan, G.; Wang, L.; Hu, Q.; Zhou, A. Synthesis Mechanisms and Thermal Stability of Ternary Carbide Mo_2Ga_2C. *Ceram. Int.* **2018**, *44*, 22289−22296.

(18) Fashandi, H.; Lai, C. C.; Dahlqvist, M.; Lu, J.; Rosen, J.; Hultman, L.; Greczynski, G.; Andersson, M.; Lloyd Spetz, A.; Eklund, P. Ti_2Au_2C and $Ti_3Au_2C_2$ Formed by Solid State Reaction of Gold with Ti_2AlC and Ti_3AlC_2. *Chem. Commun.* **2017**, *53*, 9554−9557.

(19) Lai, C. C.; Fashandi, H.; Lu, J.; Palisaitis, J.; Persson, P. O. A.; Hultman, L.; Eklund, P.; Rosen, J. Phase Formation of Nanolaminated Mo_2AuC and $Mo_2(Au_{1-x}Ga_x)_2C$ by a Substitutional Reaction within Au-Capped Mo_2GaC and Mo_2Ga_2C Thin Films. *Nanoscale* **2017**, *9*, 17681−17687.

(20) Mian, L.; You-Bing, L.; Kan, L.; Jun, L.; Per, E.; Per, P.; Johanna, R.; Lars, H.; Shi-Yu, D.; Zheng-Ren, H.; Qing, H. Synthesis of Novel MAX Phase Ti_3ZnC_2 *via* A-Site-Element-Substitution Approach. *Wuji Cailiao Xuebao* **2019**, *34*, 60−64.

(21) Nechiche, M.; Cabioc'h, T.; Caspi, E. N.; Rivin, O.; Hoser, A.; Gauthier-Brunet, V.; Chartier, P.; Dubois, S. Evidence for Symmetry Reduction in $Ti_3(Al_{1-\delta}Cu_\delta)C_2$ MAX Phase Solid Solutions. *Inorg. Chem.* **2017**, *56*, 14388−14395.

(22) Marquez, L. A.; Dunford, H. B. Mechanism of the Oxidation of 3,5,3′,5′-Tetramethylbenzidine by Myeloperoxidase Determined by Transient- and Steady-State Kinetics. *Biochemistry* **1997**, *36*, 9349−9355.

(23) Wei, H.; Wang, E. Nanomaterials with Enzyme-Like Characteristics (Nanozymes): Next-Generation Artificial Enzymes. *Chem. Soc. Rev.* **2013**, *42*, 6060−6093.

(24) Wu, J.; Wang, X.; Wang, Q.; Lou, Z.; Li, S.; Zhu, Y.; Qin, L.; Wei, H. Nanomaterials with Enzyme-Like Characteristics (Nanozymes): Next-Generation Artificial Enzymes (II). *Chem. Soc. Rev.* **2019**, *48*, 1004−1076.

(25) Porter, D. J.; Bright, H. J. The Mechanism of Oxidation of Nitroalkanes by Horseradish Peroxidase. *J. Biol. Chem.* **1983**, *258*, 9913−9924.

(26) Wei, H.; Wang, E. Fe_3O_4 Magnetic Nanoparticles as Peroxidase Mimetics and Their Applications in H_2O_2 and Glucose Detection. *Anal. Chem.* **2008**, *80*, 2250−2254.

(27) Huang, L.; Chen, J.; Gan, L.; Wang, J.; Dong, S. Single-Atom Nanozymes. *Sci. Adv.* **2019**, *5*, eaav5490.

(28) Liu, Y.; Wu, H.; Li, M.; Yin, J. J.; Nie, Z. PH Dependent Catalytic Activities of Platinum Nanoparticles with Respect to the Decomposition of Hydrogen Peroxide and Scavenging of Superoxide and Singlet Oxygen. *Nanoscale* **2014**, *6*, 11904−11910.

(29) Ling, Y.; Zhang, N.; Qu, F.; Wen, T.; Gao, Z. F.; Li, N. B.; Luo, H. Q. Fluorescent Detection of Hydrogen Peroxide and Glucose with Polyethyleneimine-Templated Cu Nanoclusters. *Spectrochim. Acta, Part A* **2014**, *118*, 315−320.

DOI: 10.1021/acsnano.9b03530
ACS Nano 2019, 13, 9198−9205

(30) Huang, J.; Zhu, Y.; Zhong, H.; Yang, X.; Li, C. Dispersed CuO Nanoparticles on a Silicon Nanowire for Improved Performance of Nonenzymatic H_2O_2 Detection. *ACS Appl. Mater. Interfaces* **2014**, *6*, 7055−7062.
(31) Hu, L.; Yuan, Y.; Zhang, L.; Zhao, J.; Majeed, S.; Xu, G. Copper Nanoclusters as Peroxidase Mimetics and Their Applications to H_2O_2 and Glucose Detection. *Anal. Chim. Acta* **2013**, *762*, 83−86.
(32) Wang, F.; Liu, X.; Lu, C.-H.; Willner, I. Cysteine-Mediated Aggregation of Au Nanoparticles: the Development of a H_2O_2 Sensor and Oxidase-Based Biosensors. *ACS Nano* **2013**, *7*, 7278−7286.
(33) Xu, F.; Sun, Y.; Zhang, Y.; Shi, Y.; Wen, Z.; Li, Z. Graphene-Pt Nanocomposite for Nonenzymatic Detection of Hydrogen Peroxide with Enhanced Sensitivity. *Electrochem. Commun.* **2011**, *13*, 1131−1134.
(34) Wu, S.; Zhao, H.; Ju, H.; Shi, C.; Zhao, J. Electrodeposition of Silver−DNA Hybrid Nanoparticles for Electrochemical Sensing of Hydrogen Peroxide and Glucose. *Electrochem. Commun.* **2006**, *8*, 1197−1203.
(35) Zhou, P.; Dai, Z.; Fang, M.; Huang, X.; Bao, J.; Gong, J. Novel Dendritic Palladium Nanostructure and Its Application in Biosensing. *J. Phys. Chem. C* **2007**, *111*, 12609−12616.
(36) Clark, S. J.; Segall, M. D.; Pickard, C. J.; Hasnip, P. J.; Probert, M. I. J.; Refson, K.; Payne, M. C. First Principles Methods Using CASTEP. *Z. Kristallogr. - Cryst. Mater.* **2005**, *220*, 567−570.
(37) Segall, M. D.; Lindan, P. J. D.; Probert, M. J.; Pickard, C. J.; Hasnip, P. J.; Clark, S. J.; Payne, M. C. First-Principles Simulation: Ideas, Illustrations and the CASTEP Code. *J. Phys.: Condens. Matter* **2002**, *14*, 2717−2744.
(38) Perdew, J. P.; Burke, K.; Ernzerhof, M. Generalized Gradient Approximation Made Simple. *Phys. Rev. Lett.* **1996**, *77*, 3865−3868.
(39) Perdew, J. P.; Chevary, J. A.; Vosko, S. H.; Jackson, K. A.; Pederson, M. R.; Singh, D. J.; Fiolhais, C. Erratum: Atoms, Molecules, Solids, and Surfaces: Applications of the Generalized Gradient Approximation for Exchange and Correlation. *Phys. Rev. B: Condens. Matter Mater. Phys.* **1992**, *46*, 6671−6687.
(40) Kohn, W.; Sham, L. J. Self-Consistent Equations Including Exchange and Correlation Effects. *Phys. Rev.* **1965**, *140*, A1133−A1138.
(41) Vanderbilt, D. Soft Self-Consistent Pseudopotentials in a Generalized Eigenvalue Formalism. *Phys. Rev. B: Condens. Matter Mater. Phys.* **1990**, *41*, 7892−7895.
(42) Frank, W.; Elsasser, C.; Fahnle, M. *Ab initio* Force-Constant Method for Phonon Dispersions in Alkali Metals. *Phys. Rev. Lett.* **1995**, *74*, 1791−1794.
(43) Parlinski, K.; Li, Z. Q.; Kawazoe, Y. First-Principles Determination of the Soft Mode in Cubic ZrO_2. *Phys. Rev. Lett.* **1997**, *78*, 4063−4066.
(44) Fang, C. M.; Ahuja, R.; Eriksson, O.; Li, S.; Jansson, U.; Wilhelmsson, O.; Hultman, L. General Trend of the Mechanical Properties of the Ternary Carbides M_3SiC_2 (M = Transitionmetal). *Phys. Rev. B: Condens. Matter Mater. Phys.* **2006**, *74*, No. 054106.

DOI: 10.1021/acsnano.9b03530
ACS Nano 2019, 13, 9198−9205